

1 **Behaviour of iron isotopes in hydrothermal systems: Beebe and Von Damm**
2 **vent fields on the Mid-Cayman ultraslow-spreading ridge**

3

4 **Wenhao Wang¹, Alastair Lough¹, Maeve C. Lohan¹, Douglas P. Connelly², Matthew**
5 **Cooper¹, J. Andy Milton¹, Valerie Chavagnac³, Alain Castillo³, Rachael H. James¹**

6 ¹ School of Ocean and Earth Science, University of Southampton, Southampton, UK

7 ² Marine Geosciences, National Oceanography Centre, Southampton, UK

8 ³ Geosciences Environment Toulouse, CNRS-UMR5563, University of Toulouse, Toulouse, France

9

10

11 **Abstract**

12 It is now clear that, in some parts of the ocean, inputs of hydrothermal iron (Fe) can make a
13 more significant contribution to the Fe inventory than previously thought. While the Fe isotopic
14 signature of seawater has proved useful for distinguishing between inputs of Fe from
15 atmospheric deposition and seafloor sediments, the Fe isotope signature of hydrothermal vent
16 fluids may change during mixing of vent fluids and seawater. To better constrain the processes
17 leading to these changes, the Fe isotopic compositions ($\delta^{56}\text{Fe}$) of dissolved and total dissolvable
18 Fe have been determined in high temperature vent fluids and the buoyant hydrothermal plumes
19 at the Beebe and the Von Damm vent fields, which are located along the ultraslow Mid-Cayman
20 spreading centre in the Caribbean Sea.

21 Our results show that the $\delta^{56}\text{Fe}$ value of dissolved Fe in the earliest stages of buoyant plume
22 formation was lower (as low as -4.08%) than measured in a high temperature, low-Mg, vent
23 fluid sample (-0.28%). This indicates that the iron isotopic signature of dissolved Fe is
24 principally controlled by oxidation of Fe(II) and precipitation of Fe-(oxyhydr)oxides that

25 preferentially incorporate heavy Fe isotopes. In support of this, the $\delta^{56}\text{Fe}$ value of labile
26 particulate Fe was higher than the $\delta^{56}\text{Fe}$ value of dissolved Fe. Nevertheless, at Beebe, the $\delta^{56}\text{Fe}$
27 value of total dissolvable Fe increased as the proportion of Fe predicted to have been lost from
28 the plume increased, consistent with preferential fall-out of Fe-sulfides that are enriched in
29 light Fe isotopes. The very low $\delta^{56}\text{Fe}$ values of dissolved Fe in the Beebe buoyant plume are
30 consistent with (i) the high Fe/H₂S ratio of the vent fluids, and (ii) high Fe(II) oxidation rates,
31 relative to other vent sites.

32

33 **Key words**

34 Iron isotopes, Hydrothermal plumes, Vent fluids, Beebe, Von Damm

35

36 **1 Introduction**

37 Iron (Fe) plays a key role in the oceanic carbon cycle because it regulates primary productivity
38 in some parts of the world's ocean (*Boyd et al., 2007*). In those parts of the ocean where Fe is
39 limiting, levels of the major nutrients (nitrate, phosphate and silicate) are high, which means
40 that the operation of the carbon pump is highly inefficient and sequestration of atmospheric
41 CO₂ is restricted (*Watson et al., 2000*). Determining and quantifying the main sources of Fe to
42 the ocean is therefore critical. However, the relative contributions of different sources of Fe to
43 the oceans remain uncertain as flux estimates from atmospheric dust, oceanic sediments and
44 hydrothermal venting vary by orders of magnitude (*Tagliabue et al., 2010*).

45 Instrumental and methodological developments over the last two decades mean that it is now
46 possible to accurately determine the stable isotope ratios of dissolved Fe in seawater, which
47 facilitates 'fingerprinting' of Fe from different sources. The $\delta^{56}\text{Fe}$ signature of atmospheric
48 aerosols is $\sim 0\text{‰}$, although the $\delta^{56}\text{Fe}$ value of Fe that dissolves from dust may be higher
49 ($\sim +0.68\text{‰}$, *Conway and John, 2014*). Sedimentary Fe produced by dissimilatory Fe reduction
50 carries a negative $\delta^{56}\text{Fe}$ signature (-3.3 to -1.8‰ , *Homoky et al., 2009; Severmann et al., 2006*),
51 whereas sedimentary Fe produced by non-reductive dissolution processes has a heavier $\delta^{56}\text{Fe}$
52 value, $+0.07 \pm 0.07\text{‰}$ (*Homoky et al., 2021*). The $\delta^{56}\text{Fe}$ values of hydrothermal vent fluids are
53 also distinct, ~ -0.67 to -0.12‰ (*Sharma et al., 2001; Beard et al., 2003; Severmann et al.,*
54 *2004; Rouxel et al., 2008; Bennett et al., 2009; Klar et al., 2017; Syverson et al., 2017;*
55 *Nasemann et al., 2018*), suggesting that Fe isotope signatures could be used to provide new
56 information that would help constrain the oceanic cycle of Fe.

57 It was previously assumed that hydrothermal activity is not a major source of Fe because of
58 precipitation of Fe-sulfides and Fe-(oxyhydr)oxides as Fe-rich high temperature hydrothermal
59 vent fluids mix with seawater (*German et al., 1991*). However, studies have shown that a
60 substantial portion of hydrothermal Fe may remain in the dissolved ($<0.2 \mu\text{m}$) phase (e.g.,

61 *Kleint et al., 2016*), and this Fe may be transported for thousands of kilometres away from the
62 mid-ocean ridge (*Saito et al., 2013; Fitzsimmons et al., 2014; Resing et al., 2015*). In support
63 of this, numerical modelling studies have shown improved ability to reproduce Fe distributions
64 when hydrothermal Fe sources were included (*Tagliabue et al., 2010*). However, these models
65 did not consider the distinctive behaviour of Fe within the proximal vs distal hydrothermal
66 plume, or variations in Fe fluxes from different vent sites. Extending the models to incorporate
67 these parameters, as well as increasing observations of Fe concentrations and Fe isotope
68 distributions, particularly for hydrothermal systems, is critical for providing reliable
69 predictions of future changes in the distribution of Fe and other micronutrients as well as carbon
70 export.

71 Hydrothermal plumes are created as vent fluids mix with seawater, whereby steep gradients in
72 temperature, pH and Eh lead to precipitation of metals as sulfides and oxides (*Rudnicki and
73 Elderfield, 1993*). Fe isotope fractionation associated with these Fe precipitation pathways has
74 been examined by analysis of particles within hydrothermal plumes at the Mid-Atlantic Ridge
75 (*Severmann et al., 2004; Bennett et al., 2009*) and the East Pacific Rise (*Rouxel et al., 2016*).
76 More recent process studies at the East Scotia Ridge and the Vanuatu back-arc (*Klar et al.,
77 2017; Lough et al., 2017; Nasemann et al., 2018*) have shown that significant changes in $\delta^{56}\text{Fe}$
78 values of dissolved Fe occurred during plume rise and dispersal due to precipitation of Fe-
79 sulfides and Fe-(oxyhydr)oxides that are, respectively, isotopically lighter and heavier, than
80 the residual dissolved Fe. Iron that remains in the dissolved fraction may be stabilised in the
81 form of nanoparticles and/or organic complexes (*Toner et al., 2009; Fitzsimmons et al., 2017;
82 Findlay et al., 2019*), contributing not only to the dissolved Fe budget but also the $\delta^{56}\text{Fe}$
83 signature of dissolved Fe in the wider deep ocean.

84 The aim of this study was to determine the behaviour of iron isotopes in two hydrothermal
85 systems, the Beebe vent field (BVF) and the Von Damm vent field (VDVF), located along the

86 ultraslow Mid-Cayman spreading ridge (full spreading rate $<20 \text{ mm yr}^{-1}$) that bisects the
87 Cayman Trough in the Caribbean Sea (Fig.1). This fills an important gap in knowledge,
88 because ultraslow-spreading centres are under-sampled globally, and models of hydrothermal
89 Fe inputs based on ridge spreading rates have typically assumed that vents located along
90 ultraslow-spreading ridges represent an insignificant source of Fe (Tagliabue *et al.*, 2010;
91 Resing *et al.*, 2015).

92

93 **2 Sampling sites**

94 The Beebe vent field is located at $18^{\circ}32.785'N$ $81^{\circ}43.080'W$ and in a water depth of 4960 m
95 depth on the axis of the Mid-Cayman spreading ridge. It is the deepest hydrothermal vent field
96 discovered to date, and the vent fluids are unusually buoyant such that the buoyant part of the
97 hydrothermal plume extends up to 1200m above the seabed (Connelly *et al.*, 2012).
98 Hydrothermal fluids circulate through mafic and ultramafic lithologies and the vent field
99 consists of at least six discrete sulfide mounds, three of which host active sites of fluid venting
100 (Beebe Woods, Beebe 125 and Deepest Vents). The Beebe vent field is also referred to as the
101 'Piccard' vent field in the literature; here we use the name 'Beebe' as this is the name listed in
102 the InterRidge database after venting was visually confirmed at the seafloor (Connelly *et al.*,
103 2012).

104 The Von Damm vent field is located at $18^{\circ}22.605'N$ $81^{\circ}47.875'W$ at 2300 m water depth, on
105 the upper slopes of an oceanic core complex, 13 km west of the spreading axis and ~20 km
106 away from Beebe (Fig.1). Tectonic exposure of lower crustal and upper mantle rocks gives rise
107 to a heterogeneous basement (Hodgkinson *et al.*, 2015). Particle-poor hydrothermal fluids have
108 been observed emanating from a series of talc chimneys, called Main Spire, Hotter than Hole,
109 X15 and Chimlets (Hodgkinson *et al.*, 2015).

110 The local surrounding deep seawater mass at both sites has a temperature of 3.98°C, a salinity
111 of 34.988, and an O₂ concentration of ~220 μM (*Connelly et al., 2012*), similar to North
112 Atlantic Deep Water (NADW).

113

114 **3 Methods**

115 3.1 Sample collection

116 Hydrothermal vent fluids, and fluids from the buoyant hydrothermal plume, were sampled
117 during RRS *James Cook* cruise JC82 in February 2013. Gas tight fluid samplers were employed
118 to collect vent fluid samples from different chimneys, and temperatures were measured
119 separately within the orifice using a probe deployed by the remotely operated vehicle (ROV)
120 *Isis*. The vent fluid samples were then transferred into acid-cleaned polyethylene (PE) vials
121 and were acidified on board to 0.015 M with ultra-pure nitric acid (*Romil*), for analysis back in
122 the laboratory. Any precipitates that formed in the gas-tight samplers were re-dissolved and
123 accounted for in the final element concentrations.

124 Hydrothermal plumes were detected using a Seabird 911 plus conductivity, temperature and
125 depth (CTD) profiler system together with a light scattering sensor (LSS) and an Eh electrode.
126 The buoyant part of the hydrothermal plumes was identified by positive LSS and temperature
127 anomalies and a negative Eh anomaly. At Beebe, the buoyant hydrothermal plume rises a
128 considerable distance (up to 1200 m) above the seabed (*Connelly et al., 2012*); we distinguish
129 between plume samples that have Mn concentrations of >20 nM (which represent the earliest
130 stages of buoyant plume formation) from plume samples that have Mn concentrations of <20
131 nM (which represent the latter stages of buoyant plume formation). The cut-off Mn = 20 nM
132 corresponds to a vent fluid dilution factor of ~30,000 at Beebe and ~900 at Von Damm (see
133 [Section 4.2](#)).

134 Water samples from the buoyant plume at Beebe (3-241 m above the seabed) were collected
135 using 10 L Ocean Test Equipment (OTE) water sampling bottles mounted on a titanium rosette
136 deployed from the ship. At Von Damm, plume samples were collected 1-23 m above the seabed
137 using 1.2 L OTE bottles attached to the ROV *Isis*. Both sets of OTE bottles were modified for
138 trace metal sampling and were pre-cleaned. Upon retrieval of the OTE bottles, ~500 mL of
139 unfiltered seawater was collected for analysis of total dissolvable (TD) iron and manganese
140 (Mn). The rest of the seawater sample was then filtered as soon as possible (within ~4 h of the
141 sample bottle closing) through a polycarbonate membrane filter (0.2 μm , Whatman) under
142 gentle pressure, for collection of dissolved Fe (dFe) and Mn (dMn). Note that although the
143 relatively low pH of buoyant plume waters means that the half-life for Fe(II) oxidation will be
144 substantially longer than it is in bottom seawater (0.28 h at Beebe and 0.45 h at Von Damm;
145 *Lough et al., 2019a, b*), changes in Fe speciation may have occurred between closure of the
146 sampling bottle and filtration. Both sets of samples were stored in acid-cleaned low density
147 polyethylene bottles (LDPE), and were acidified to pH ~1.8 with ultra-pure nitric acid (*Romil*).
148 Thus, dFe is defined as Fe that is retained in seawater filtered at $<0.2 \mu\text{m}$, whereas TDFe
149 consists of both dFe and Fe from the labile fraction of suspended particles (that is, Fe leached
150 by addition of 0.03 M HNO_3 during storage for >6 months). All sample bottles were bagged
151 and shipped back to the laboratory for further analysis.

152

153 3.2 Fe isotope analysis

154 The iron isotope compositions of hydrothermal vent fluids and plume samples were determined
155 using a double spike technique, adapted from *Lacan et al. (2010)*. All acids used for chemical
156 processing were thermally distilled. Milli-Q (MQ, 18.2 $\text{M}\Omega$) water was used for diluting and
157 cleaning. LDPE bottles and Perfluoroalkoxy (PFA) vials were thoroughly cleaned for trace

158 metal purposes. Samples were handled under laminar flow hoods, set within Class 100 clean
159 laboratories at the University of Southampton.

160 Hydrothermal plume samples (dissolved and total dissolvable phases) were pre-concentrated
161 using NTA Superflow (Qiagen) resin. Columns were made with PFA tubing and a polyethylene
162 (PE) frit, and loaded with ~1 mL of clean NTA resin. The sample pH was adjusted to between
163 1.7-1.8 and 10 μ M UpA-grade hydrogen peroxide (H_2O_2 , Sigma Aldrich) was added to the
164 sample ~30 min prior to starting the pre-concentration procedure. Between uses and before
165 loading a sample, the resin was cleaned with 75 mL 1.5 M HCl and 80 mL MQ. The sample
166 was passed over the resin by gravity flow, and the resin was then rinsed with MQ water to
167 remove residual salts. The Fe fraction was eluted with 10 mL of 1.5 M HCl, collected in an
168 acid cleaned PFA vial (Savillex), and subsequently evaporated on a hotplate at ~90°C and
169 reconstituted in 5M HCl (with 0.001% H_2O_2) for further analysis.

170 Iron can be efficiently separated from cations such as Cr and Ni that also bind to NTA resin,
171 by conversion to $FeCl_4^-$ in strong HCl and purification by anion exchange. Approximately 200
172 μ L of cleaned AG-MP1 resin (BioRad) was loaded in handmade micro columns (PE material,
173 ~8 cm length and ~3 mm diameter). Each column was pre-cleaned by addition of 1 mL of 2 M
174 HNO_3 and conditioned by addition of 0.2 mL of 5 M HCl (with 0.001% H_2O_2), before loading
175 the sample in 5 M HCl (with 0.001% H_2O_2). Matrix elements were eluted with 1 mL of 5 M
176 HCl (with 0.001% H_2O_2). Then the Fe fraction was eluted with 1 mL of 1 M HCl into a clean
177 Savillex vial, and was dried down gently and re-dissolved in 0.3 M HNO_3 .

178 No pre-concentration was needed for the vent fluids, as they exhibit much higher Fe
179 concentrations than plume samples. Prior to purification on the anion exchange column, the
180 vent fluid samples were oxidised by reflux with concentrated HNO_3 and H_2O_2 .

181 The Fe isotopic composition was determined by multicollector inductively coupled plasma
182 mass spectrometry (MC-ICP-MS; Thermo Fisher Neptune Plus). Instrumental mass bias was
183 corrected using a ^{57}Fe - ^{58}Fe double spike, which was added in equi-molar concentration to the
184 sample before chemical processing. The isotope values are reported in delta notation relative
185 to the Fe isotope reference material IRMM-14 and expressed as:

$$186 \quad \delta^{56}\text{Fe} (\text{‰}) = [({}^{56}\text{Fe}/{}^{54}\text{Fe})_{\text{sample}}/({}^{56}\text{Fe}/{}^{54}\text{Fe})_{\text{IRMM-14}} - 1] \times 1000 \quad (1)$$

187 Samples with $\sim 100 \text{ ng mL}^{-1}$ Fe were introduced to the plasma using an Apex-Q desolvator (ESI)
188 and signals from ^{54}Fe , ^{56}Fe , ^{57}Fe , ^{58}Fe , ^{53}Cr , ^{60}Ni were quantified. Analysis by MC-ICP-MS
189 was carried out in high-resolution mode, and each sample measurement consisted of 50
190 individual measurement cycles. The instrument was carefully tuned to give sufficient mass
191 resolution (>8000), before running a sequence that consisted of analysis of the reference
192 material (IRMM), the internal Fe standard (ETH), Sample 1, Sample 2, then back to the IRMM
193 reference material again. The wash time was 70 s before analysis of each sample/standard and
194 420 s before the analysis of blanks. The mean beam intensity of a blank solution that was
195 analysed before and after each sample/standard was subtracted. Mass bias was corrected by
196 iteratively deconvolving the spike-sample mix based on data reduction methodology (*Albarède*
197 *and Beard, 2004*). Long-term analysis of the ETH iron isotope standard gave $\delta^{56}\text{Fe} =$
198 $+0.51 \pm 0.09\text{‰}$ (2SD, $n=45$), in agreement with the consensus value ($+0.52 \pm 0.08\text{‰}$; *Lacan et*
199 *al., 2010*). We apply $\pm 0.09\text{‰}$ as an estimate of reproducibility of the $\delta^{56}\text{Fe}$ values for all
200 samples in this study.

201 The overall procedural (preconcentration and purification) Fe blank was $1.54 \pm 0.74 \text{ ng}$ ($n=2$).
202 The accuracy of the method was validated through the analysis of trace metal free seawater
203 doped with the hematite (HEM) iron isotope standard, yielding an average $\delta^{56}\text{Fe}$ value of
204 $+0.22 \pm 0.10\text{‰}$ (2SD, $n=5$), consistent with previously published HEM values ($\delta^{56}\text{Fe} =$
205 $+0.24 \pm 0.05\text{‰}$; *Klar et al., 2017*).

206

207 3.3 Ancillary analyses

208 The vent fluids were diluted 100-2500 fold with 0.3 M HNO₃ and concentrations of major and
209 minor cations were determined by inductively coupled plasma atomic adsorption spectroscopy
210 (ICP-AES; iCAP 6000, Thermo Scientific) and ICP-MS (X-series, Thermo Scientific).
211 Chloride (Cl) concentrations were measured by ion chromatography (Dionex), and hydrogen
212 sulfide was measured immediately after recovery of the gas tight fluid sampler by iodometric
213 titration.

214 The Fe and Mn concentrations in the hydrothermal plume samples were measured by ICP-MS
215 (Element XR, Thermo Scientific) after pre-concentration on a chelating resin using an offline
216 extraction system as discussed in *Lough et al. (2019a)* and *Lough et al. (2019b)*. The initial
217 determinations of dissolved and total dissolvable Fe (dFe and TDFe) concentrations were used
218 to estimate the sample volume required for ~100 ng of Fe for the isotopic analysis.

219 The reported Fe concentration data are from the MC-ICP-MS measurements. Iron
220 concentrations were determined simultaneously with the isotope ratio measurements via
221 isotope dilution equations, based on the known sample volume and the quantity of added spike.
222 The uncertainty of these measurements was less than ±1%. The MC-ICP-MS data were within
223 20% (with two exceptions) of the concentration measured by ICP-MS.

224

225 **4 Results**

226 4.1 Hydrothermal vent fluids

227 The chemical compositions of vent fluid samples analysed for δ⁵⁶Fe are shown in [Table 1](#), and
228 the compositions of all vent fluid samples collected on cruise JC82 are given in the
229 [Supplementary Information \(Table S1\)](#). At Beebe, the vent fluids had relatively high

230 temperatures (350 to 401 °C) and low pH (2.9 to 3.1) compared to vent fluids from Von Damm
231 (temperatures up to 215 °C and pH = ~6-7).

232 The sampled vent fluid compositions can be assumed to reflect two-component mixing of a
233 hydrothermal ‘end-member’ fluid that contains no magnesium (Mg) with bottom seawater
234 (*Bischoff and Dickson, 1975*). Based on this assumption, the samples analysed for $\delta^{56}\text{Fe}$ from
235 Beebe consisted of >90% hydrothermal fluid, whereas the sample from Von Damm with lowest
236 Mg consisted of ~70% hydrothermal fluid. Vent fluid samples with low Mg (as low as 2.5 mM)
237 have nevertheless been collected from Von Damm during other sampling campaigns
238 (*McDermott, 2015*).

239 Based on the extended vent fluid data ([Table S1](#)), and by extrapolation to zero-Mg, the
240 hydrothermal end-member Mn and Fe concentrations at the Beebe vent field were, respectively,
241 597 ± 10.4 (Beebe 125) to 618 ± 6.0 μM (Deepest Vents) and 6320 ± 209 (Beebe 125) to
242 8150 ± 1990 μM (Deepest Vents), similar to end-member fluid compositions ($567\text{-}571$ μM Mn
243 and $6660\text{-}12800$ μM Fe) reported by *McDermott et al. (2018)* for the same study area. The
244 estimated end-member H_2S concentrations (3.8 ± 0.34 mM (Beebe 125) to 6.8 ± 1.0 mM
245 (Deepest Vents)) were lower than measured previously (~12 mM; *McDermott et al., 2018*).
246 Estimated end-member Cl concentrations (366 ± 5.8 mM for Beebe 125 and 364 ± 2.6 mM for
247 Deepest Vents) were lower than background seawater (~550 mM), which has been attributed
248 to phase separation (*McDermott et al., 2018*).

249 Using the same methodology, the end-member vent fluids from Main Spire at the Von Damm
250 vent field had Mn = 11.6 ± 0.44 μM and Fe = 22.5 ± 4.2 μM , within the range ($8.9\text{-}11.3$ μM for
251 Mn and $21\text{-}46$ μM for Fe) of low Mg (2.5-14.8 mM) fluids reported by *McDermott (2015)*. As
252 no samples with low Mg concentrations were collected at Hotter than Hole and Chimlet 2, we
253 could only estimate minimum values for the end-member contents for non-conservative
254 elements; for Mn the minimum value was 22.5 ± 4.2 μM and for Fe the minimum value was

255 412±137 μM. The minimum end-member H₂S concentrations were ~1.6±0.3 mM for Main
256 Spire and ~1.2±0.5 mM for Hotter than Hole and Chimlet 2, slightly lower than values reported
257 for low Mg vent fluids from East Summit (3.3 mM; *McDermott, 2015*). The estimated end-
258 member chloride contents of the Von Damm vent fluids (686±26 mM for Main Spire, 681±12
259 mM for Hotter than Hole and Chimlet 2) were slightly higher than background seawater (~546
260 mM), which has been attributed to hydration reactions during serpentinization that remove
261 water from the circulating fluids (*Hodgkinson et al., 2015*).

262 At the Beebe vent field, the sample with lowest Mg had a δ⁵⁶Fe value of -0.28‰, within the
263 range of high-temperature fluids from basalt-hosted hydrothermal fields on the Mid-Atlantic
264 Ridge (-0.5 to -0.2‰; *Bennett et al., 2009; Severmann et al. 2004*). At the Von Damm vent
265 field, the δ⁵⁶Fe value of the fluid sample with lowest Mg was slightly higher, +0.08‰.

266

267 4.2 Dissolved and total dissolvable Fe concentrations in the buoyant hydrothermal plumes

268 The dFe and TDFe concentrations in buoyant plume samples from the Beebe and Von Damm
269 vent fields are plotted against the vent fluid dilution factor in [Fig. 2a](#). The vent fluid (VF)
270 dilution factor is given by $([\text{Mn}]_{\text{VF}} - [\text{Mn}]_{\text{SW}})/([\text{Mn}]_{\text{sample}} - [\text{Mn}]_{\text{SW}})$, where [Mn] represents
271 Mn concentration and SW represents background seawater. [Mn]_{VF} was 597-618 μM for Beebe
272 and 11.6-22.5 μM for Von Damm ([Table 1](#)), and [Mn]_{SW} was 0.1 nM (*Lough et al., 2019a*).
273 The VF dilution factor varied between ~3,000 and 70,000 at Beebe, whereas between ~60 and
274 10,000 at Von Damm. As Mn shows near-conservative behaviour during mixing of vent fluids
275 and seawater over timescales of weeks, it therefore serves as a tracer of hydrothermal plume
276 dispersal on the spatial scale that we sampled.

277 At both vent fields, concentrations of TDFe and dFe were lower at higher VF dilution factor
278 ([Fig. 2a](#)), as the hydrothermal fluids mix with background seawater with low Fe. At Beebe,

279 concentrations of TDFe were ~30-73% (average $53\pm 15\%$) lower than predicted for
280 conservative mixing between the vent fluid and seawater, indicating that Fe was removed from
281 the TD fraction, most likely by fall-out of sulfide particles as soon as the vent fluids were
282 expelled at the seabed (*Rudnicki and Elderfield, 1993; Lough et al., 2019a*). However, at Von
283 Damm, concentrations of TDFe in the plume were generally within the range predicted by
284 conservative mixing, suggesting that particle fall-out at this site was minimal (*Lough et al.,*
285 *2019b*).

286 Concentrations of dFe at Beebe and Von Damm, respectively, ranged from 16.1 to 86.5 nM
287 and 21.0 to 62.6 nM. These values are significantly higher than background seawater (0.77 nM
288 in the Cayman Trench; *Lough et al., 2019a*). In general, the ratio of dFe/TDFe increased as the
289 plume became more dilute, varying from $< \sim 10\%$ in the earliest stages of buoyant plume
290 formation to up to $\sim 60\%$ at higher VF dilution factors. Thus, a higher proportion of Fe is present
291 in the labile particulate fraction close to the vent source.

292

293 4.3 Isotopic composition of dFe and TDFe in the buoyant hydrothermal plumes

294 The $\delta^{56}\text{Fe}$ values of dFe showed notable changes as the buoyant plume became more dilute
295 ([Fig. 2b](#); [Table S2](#)). At the Beebe vent field, samples from the least dilute part of the plume had
296 very low $\delta^{56}\text{Fe}$ values (as low as -4.08‰), indicating enrichment of light Fe isotopes relative
297 to the end-member vent fluid. At the Von Damm vent field, $\delta^{56}\text{Fe}$ values of dFe were as low
298 as -2.49‰ . These dFe isotope compositions are lighter than those reported for plume samples
299 recovered from the Mid-Atlantic Ridge, East Scotia Ridge, East Pacific Rise, and the Vanuatu
300 back-arc basin (-2.39 to -0.13‰ ; *Conway and John et al., 2014; Klar et al., 2017; Lough et*
301 *al., 2017; Fitzsimmons et al., 2017; Nasemann et al., 2018*). As the plumes became more dilute,

302 the $\delta^{56}\text{Fe}$ values of dFe increased; samples with the lowest dMn concentrations (9 nM and 2
303 nM) had $\delta^{56}\text{Fe}$ values of +0.29‰ and +0.22‰ at Beebe and Von Damm, respectively.

304 The $\delta^{56}\text{Fe}$ value of TDFe showed less variation during plume mixing, ranging from -0.22 to
305 +0.42‰ at both sites (Fig. 2b; Table S2). The average $\delta^{56}\text{Fe}$ value of TDFe in the Beebe plume
306 (+0.11‰) was higher than that in the Von Damm plume (-0.07‰), and higher than the $\delta^{56}\text{Fe}$
307 value of the low-Mg Beebe vent fluid (-0.28‰). At Von Damm, the $\delta^{56}\text{Fe}$ value of the vent
308 fluid with lowest Mg (+0.08‰) was within the range of $\delta^{56}\text{Fe}$ values of TDFe (-0.22 to
309 +0.13‰) measured in the plume.

310 The concentration of labile particulate Fe (LPFe) was determined from the difference in the
311 concentrations of TDFe and dFe. The Fe isotopic composition of LPFe can then be estimated
312 by mass balance. $\delta^{56}\text{Fe}$ values of LPFe ranged from +0.09 to +0.71‰ in the Beebe plume and
313 were highest during the early stages of buoyant plume formation (VF dilution factor < 30,000).
314 At Von Damm, $\delta^{56}\text{Fe}$ values of LPFe ranged from -0.38 to +0.48‰ but there was no obvious
315 shift in LPFe $\delta^{56}\text{Fe}$ values as the plume became more dilute.

316

317 4.4 Incubation experiment

318 To investigate how concentrations of dFe and $\delta^{56}\text{Fe}$ values of dFe may evolve over time, an
319 on-board incubation experiment was carried out. One 10 L water sample (sample JC82-
320 CTD11-N4) from the buoyant plume from the Beebe vent field was stored at 5°C in its OTE
321 sampling bottle for between 6 to 16 h after the sample bottle was closed before it was filtered.
322 Over this time period, the concentration of dMn stayed the same (22 ± 0.5 nmol/kg; *Lough et*
323 *al.*, 2019a), but the concentration of dFe decreased from 28.9 nM to 7.4 nM (Table S3). Over
324 the same time interval, the $\delta^{56}\text{Fe}$ value of dFe increased from -0.37‰ to +0.51‰. These data

325 indicate that, for this buoyant plume sample, isotopically light Fe was being removed from the
326 dissolved fraction over time.

327

328 **5 Discussion**

329 5.1 Fe isotope composition of the hydrothermal vent fluids

330 The $\delta^{56}\text{Fe}$ values of the low-Mg Beebe vent fluids ranged from -0.28 to -0.10‰ , within the
331 range of low-Mg hydrothermal fluids from ultramafic- and basalt-hosted hydrothermal systems
332 measured from around the world to date (-0.67 to -0.12‰ ; [Table S4](#)). These values are
333 systematically lower than unaltered mid-ocean ridge basalt ($\delta^{56}\text{Fe} = +0.1 \pm 0.01\text{‰}$; *Teng et al.*,
334 *2013*), which has been attributed to preferential leaching of light Fe isotopes during alteration
335 (*Rouxel et al.*, *2008*). Other processes, such as secondary mineral formation in the reaction
336 zone and Fe-sulfide precipitation in the shallow seafloor, may also cause fractionation of
337 Fe isotopes (*Rouxel et al.*, *2003*; *Rouxel et al.*, *2004*), but phase separation and variations in
338 host rock lithology appear to be a minor control on the Fe isotope composition of vent fluids
339 (*Beard et al.*, *2003*; *Bennett et al.*, *2009*; *Syverson et al.*, *2014*).

340 At the Von Damm vent field, the $\delta^{56}\text{Fe}$ values of vent fluids range from -0.90 to $+0.08\text{‰}$, and
341 the values decrease with increasing Mg. The sample with the lowest Mg (14.5 mM) is
342 isotopically heavy ($\delta^{56}\text{Fe} = +0.08\text{‰}$) relative to fluids from other hydrothermal sites that have
343 a low Mg content ([Table S4](#)). The hydrothermal fluids likely underwent mixing with seawater
344 circulating in the shallow subsurface prior to venting (*McDermott*, *2015*; *Hodgkinson et al.*,
345 *2015*). In these circumstances, a fraction of Fe from the hydrothermal fluid may precipitate as
346 Fe-sulfides that are preferentially enriched in light Fe isotopes (*Butler et al.*, *2005*; *Syverson et*
347 *al.*, *2013*), leaving the residual Fe isotopically heavier. The combined effects of subsurface
348 conductive cooling of hydrothermal fluids and mixing with seawater, leading to precipitation

349 of sulfides with low $\delta^{56}\text{Fe}$ values of -2 to -1% , have previously been documented at the Lucky
350 Strike vent field on the Mid-Atlantic Ridge (*Rouxel et al., 2004*).

351

352 5.2 Impact of iron precipitation on Fe isotopes as Beebe vent fluids are expelled at the seafloor

353 As discussed in [Section 4.2](#), when the hot Fe- and H_2S -rich Beebe vent fluids come into contact
354 with cold seawater, some part of the Fe appears to immediately precipitate, most likely as Fe-
355 sulfide (FeS and FeS_2 ; *Rudnicki and Elderfield, 1993*). Precipitation of Fe-sulfide would leave
356 the residual dFe enriched in the heavier Fe isotopes (*Butler et al., 2005*) and, based on analyses
357 of buoyant plume particles, the estimated difference between the $\delta^{56}\text{Fe}$ value of the Fe-sulfide
358 particles and dissolved Fe ($\delta^{56}\text{Fe}_{\text{FeS}} - \delta^{56}\text{Fe}_{\text{dFe}}$) is -0.60% (*Bennett et al., 2009*). The $\delta^{56}\text{Fe}$
359 value of the Fe remaining in the dissolved phase after sulfide precipitation (Equation 2), and
360 the accumulated Fe-sulfide precipitates (Equation 3), can be estimated using a Rayleigh
361 fractionation model:

$$362 \quad \delta^{56}\text{Fe}_{\text{dFe}} = (\delta^{56}\text{Fe}_{\text{VF}} + 1000) \cdot f^{\alpha-1} - 1000 \quad (2)$$

$$363 \quad \delta^{56}\text{Fe}_{\text{FeS}} = (\delta^{56}\text{Fe}_{\text{VF}} + 1000) \cdot \frac{1-f^\alpha}{1-f} - 1000 \quad (3)$$

364 where $\delta^{56}\text{Fe}_{\text{VF}}$ is the Fe isotope composition of the end-member vent fluid, α is the fractionation
365 factor between FeS and dFe (~ 0.9994 ; assuming $\alpha \approx e^{\delta^{56}\text{Fe}_{\text{FeS}} - \delta^{56}\text{dFe}}$), and f is the proportion
366 of Fe that remains in the dissolved phase, based on the ratios of measured to calculated TDFe
367 concentrations ([Table S2](#)).

368 While sulfide particles have not been observed in the buoyant plume at Von Damm (*Lough et*
369 *al., 2019b*), at Beebe, f has an average value of ~ 0.47 , meaning that close to 50% of the vent
370 fluid Fe precipitated as soon as the vent fluids emerged at the seabed ([Section 4.2](#)). If all of the
371 dFe lost as the vent fluids emerged at the seabed was precipitated as FeS, and given that $\delta^{56}\text{Fe}_{\text{VF}}$

372 = -0.28% , then the $\delta^{56}\text{Fe}$ value of the residual dissolved Fe would be $\sim+0.17\%$, far higher
373 than the values measured in the samples collected during the early stages of plume formation
374 (-4.08 to -1.43%).

375

376 5.3 Fractionation of Fe isotopes in the buoyant plume due to Fe(II)-Fe(III) oxidation

377 The $\delta^{56}\text{Fe}$ values of dFe in the buoyant plume samples are lower than that of Fe in the
378 hydrothermal fluid and evolve towards higher $\delta^{56}\text{Fe}$ with increasing plume dilution (Fig. 2b).
379 This strongly suggests that the iron isotopic signature of dFe in the buoyant plume samples was
380 principally controlled by oxidation of Fe(II) to Fe(III) as the vent fluids mix with oxygenated
381 seawater. Experimental and theoretical studies have shown that oxidation of $\text{Fe(II)}_{\text{aq}}$ enriches
382 heavy Fe isotopes in $\text{Fe(III)}_{\text{aq}}$, and the difference between $\delta^{56}\text{Fe(III)}_{\text{aq}}$ and $\delta^{56}\text{Fe(II)}_{\text{aq}}$ can be up
383 to 3.56% (Welch *et al.*, 2003; Anbar *et al.*, 2005). $\text{Fe(III)}_{\text{aq}}$ is not stable in seawater and forms
384 (i) colloidal (operationally defined as between 0.02 and $0.2 \mu\text{m}$ diameter) Fe-(oxyhydr)oxides
385 (FeOOH), which subsequently aggregate and coagulate into larger particles ($>0.2 \mu\text{m}$), and/or
386 (ii) organically-bound Fe(III). The proportion of organically-bound Fe(III) relative to FeOOH
387 has however been shown to be negligible in hydrothermal plumes within ~ 100 km of a vent
388 field (Fitzsimmons *et al.*, 2017). Under equilibrium conditions, the fractionation between
389 $\text{Fe(II)}_{\text{aq}}$ and FeOOH is very similar to that between $\text{Fe(II)}_{\text{aq}}$ and $\text{Fe(III)}_{\text{aq}}$, meaning that there is
390 no or very limited isotope fractionation between $\text{Fe(III)}_{\text{aq}}$ and FeOOH (Wu *et al.*, 2011).
391 Therefore, the overall effect of oxidation of Fe(II) to Fe(III) and the formation of Fe-
392 (oxyhydr)oxides is the preferential removal of the heavier Fe isotopes from the dissolved Fe
393 pool.

394 Assuming the variation in the Fe isotope composition of dFe is controlled by Fe(oxyhydr)oxide
395 formation, then the $\delta^{56}\text{Fe}$ value of dFe in the buoyant plume is a function of the proportion (F)

396 of dFe remaining as Fe(II) and the proportion (X) of Fe(III) remaining in the dissolved
 397 (colloidal) fraction. This can be modelled as a Rayleigh fractionation process as follows (*Klar*
 398 *et al., 2017; Lough et al., 2017; Nasemann et al., 2018*):

$$399 \quad \delta^{56}\text{Fe(II)} = (\delta^{56}\text{Fe(II)}_0 + 1000) \cdot F^{\alpha-1} - 1000 \quad (4)$$

$$400 \quad \delta^{56}\text{Fe(III)} = (\delta^{56}\text{Fe(II)}_0 + 1000) \cdot \frac{1-F^\alpha}{1-F} - 1000 \quad (5)$$

401 where $\delta^{56}\text{Fe(II)}$ is the isotopic composition of the remaining Fe(II), $\delta^{56}\text{Fe(II)}_0$ is the initial
 402 isotopic composition of dissolved Fe(II) before oxidation starts, $\delta^{56}\text{Fe(III)}$ is the iron isotopic
 403 composition of the accumulated Fe(III) precipitate, and α is the fractionation factor between
 404 aqueous Fe(II) and precipitated Fe(III) ($\alpha_{\text{Fe(III)-Fe(II)}} \sim 1.0035$ at a temperature of 4°C; *Welch et*
 405 *al., 2003*). The initial isotopic composition of dissolved Fe(II) before oxidation starts is the
 406 $\delta^{56}\text{Fe}$ value of Fe in the vent fluid at Von Damm (i.e. $\delta^{56}\text{Fe(II)}_0 = +0.08\text{‰}$) but, at Beebe,
 407 because ~50% of the vent fluid Fe immediately precipitates as the vent fluids are expelled at
 408 the seabed, $\delta^{56}\text{Fe(II)}_0 \approx +0.17\text{‰}$ ([Section 5.2](#)). Assuming that FeOOH precipitates at a constant
 409 rate, the $\delta^{56}\text{Fe}$ value of dFe delivered to the plume is given by (*Klar et al., 2017*):

$$410 \quad \delta^{56}\text{Fe} = \frac{F \cdot \delta^{56}\text{Fe(II)} + X \cdot (1-F) \cdot \delta^{56}\text{Fe(III)}}{F + X \cdot (1-F)} \quad (6)$$

411 Based on the measured ratios of dFe/TDFe in the buoyant plume samples with [Mn] >20 mM,
 412 the proportion of Fe(III) that precipitated can be estimated, and was $\geq 83\%$ at Beebe and $\geq 78\%$
 413 at Von Damm. As Fe(II) must reside exclusively in the dissolved fraction then the proportion
 414 of Fe(II) that is oxidised to Fe(III) must also be $\geq 78\%$. The results of this modelling exercise
 415 are shown in [Fig. 3a](#). The low $\delta^{56}\text{Fe}$ values (-4.08 to -0.60‰) in the least dilute buoyant plume
 416 samples are well described by the Rayleigh model: the lowest $\delta^{56}\text{Fe}$ value, -4.08‰ at Beebe,
 417 is consistent with oxidation of ~94% Fe(II) to Fe(III) followed by precipitation of ~89% Fe(III)
 418 as FeOOH, which is consistent with our measured concentrations of dFe and TDFe.

419 As the buoyant plumes become more dilute (lower Mn concentration), $\delta^{56}\text{Fe}$ values of dFe
420 increase (to +0.22 to +0.29‰). This can be partly explained by near-quantitative oxidation of
421 Fe(II), but it is also consistent with: (i) exchange of Fe between the particulate and dissolved
422 fractions, whereby isotopically heavy Fe is re-released from Fe-(oxyhydr)oxides (*Fitzsimmons*
423 *et al.*, 2017; *Lough et al.*, 2019a, 2019b); and/or (ii) an increase in the proportion of dFe that
424 is complexed by organic ligands (*Fitzsimmons et al.*, 2017) as organically bound Fe(III) is
425 isotopically heavy relative to unbound Fe(III) by up to +0.6‰ (*Dideriksen et al.*, 2008; *Morgan*
426 *et al.*, 2010).

427

428 5.4 Behaviours of Fe-sulfide and Fe-(oxyhydr)oxide particles in the buoyant plume

429 While precipitation of Fe-(oxyhydr)oxides (that preferentially incorporate heavy Fe isotopes)
430 is the principal control on the iron isotopic composition of dFe delivered to the buoyant plume
431 ([Section 5.3](#)), we note that the $\delta^{56}\text{Fe}$ value of TDFe increases as the proportion of Fe predicted
432 to have been lost from the plume increases ([Fig. 3b](#)). This suggests that Fe loss from the
433 buoyant plume primarily occurs via fall-out of Fe-sulfides that are relatively enriched in light
434 Fe isotopes. Fe-sulfide particles are relatively dense compared to Fe-(oxyhydr)oxides and will
435 settle out of the plume more quickly (*Lough et al.*, 2017).

436 By contrast, Fe-(oxyhydr)oxides have relatively small particle size and tend to remain in the
437 plume after they form (*Fitzsimmons et al.*, 2017; *Lough et al.*, 2019a). In support of this,
438 calculated $\delta^{56}\text{Fe}$ values of the labile particulate fraction (LPFe) are higher (−0.13 to +0.71‰)
439 in the earliest stages of buoyant plume formation than the $\delta^{56}\text{Fe}$ values of dFe. The calculated
440 $\delta^{56}\text{Fe}$ values of LPFe are generally similar to or slightly lower than the $\delta^{56}\text{Fe}$ values of the
441 accumulated Fe(III) precipitate predicted by Rayleigh modelling ([Fig. 3a](#)). The slightly lower
442 than predicted LPFe $\delta^{56}\text{Fe}$ values, at least at Beebe, may be due to the presence of Fe-sulfides

443 in the labile particulate fraction, but we also note that weak acid leaching of natural particles
444 may fractionate Fe isotopes to a small extent (e.g., *Dunlea et al., 2021*).

445

446 5.5 Evidence for coagulation of Fe-sulfide nanoparticles in the buoyant plume

447 Results of the incubation experiment show that the concentration of dFe in the buoyant plume
448 sample progressively decreased over time whereas the $\delta^{56}\text{Fe}$ values of dFe increased ([Fig. 4a](#)),
449 consistent with preferential loss of light Fe isotopes from the dissolved fraction. As the half-
450 life for Fe(II) oxidation at Beebe is short (0.28 h; *Lough et al., 2019a*), Fe(II) oxidation was
451 essentially complete by the time the first sub-sample was collected 6 hours after the sample
452 bottle was closed (see [Section 4.4](#)). This means that changes in $\delta^{56}\text{Fe}$ values cannot be attributed
453 to Fe(II) oxidation which, in any case, would remove Fe that is preferentially enriched in heavy
454 Fe isotopes, decreasing (rather than increasing) the $\delta^{56}\text{Fe}$ value of Fe that remains in the
455 dissolved fraction.

456 The $\delta^{56}\text{Fe}$ value of accumulated Fe-sulfides in the Beebe buoyant plume was estimated to be
457 -0.68‰ (Equation 3, $f = \sim 0.47$). If removal of dFe in the incubation experiment occurred solely
458 via progressive coagulation of Fe-sulfides that are presumably in the form of nanoparticles
459 (constituting at least $\sim 75\%$ of the dFe fraction), and assuming there was no isotope
460 fractionation between coagulated Fe-sulfide particles and the remaining dFe, then mass balance
461 calculations ([Table S3](#)) indicate that the $\delta^{56}\text{Fe}$ value of dissolved Fe should increase as the
462 proportion of Fe that remains in the dissolved fraction decreases, consistent with our
463 observations ([Fig. 4c](#)). Whilst sulfide formation must have occurred before Fe oxidation starts
464 (e.g. *Rudnicki and Elderfield, 1993*) and accounts for $\sim 50\%$ loss of hydrothermal Fe(II) as the
465 vent fluids are expelled at the seabed, our incubation experiment indicates that nanoparticulate
466 Fe-sulfides can be retained in the dissolved Fe pool as the plume evolves, coagulating and

467 settling out of the plume over time. In support of this, SEM-EDX images of particles from the
468 Beebe plume have revealed the presence of large ($\sim 10 \mu\text{m}$) FeS_2 particles likely derived from
469 precipitation and coagulation of nanoparticulate FeS_2 ($< 0.2 \mu\text{m}$) that formed as the vent fluids
470 emerged at the seabed (*Lough et al., 2019a*). Formation of FeS_2 nanoparticles has also been
471 directly observed in nascent plumes forming above high-temperature vents at the East Pacific
472 Rise (*Yücel et al., 2011; Findlay et al., 2019*).

473 There is some evidence that scavenging of dFe also increases the $\delta^{56}\text{Fe}$ value of Fe that remains
474 in the dissolved fraction, by up to $\sim 0.3\text{‰}$ (e.g., *John and Adkins, 2012*). Scavenging could
475 explain the $\delta^{56}\text{Fe}$ value of the second sub-sample that was collected ~ 8 h after the sample bottle
476 was closed (*Fig. 4d*), but the rest of the incubation experiment data are more consistent with
477 loss of dFe due to coagulation of Fe-sulfide nanoparticles (*Fig. 4c*). Finally, we note that our
478 incubation experiment data are not consistent with coagulation and precipitation of organically-
479 bound Fe(III) colloids that are isotopically heavy relative to unbound Fe(III) (and Fe(II))
480 (*Dideriksen et al., 2008; Morgan et al., 2010; Fitzsimmons et al., 2017*).

481 By contrast, a similar incubation experiment carried out on a buoyant plume sample collected
482 from the E2 hydrothermal site on the East Scotia Ridge (*Lough et al., 2017*) revealed that while
483 dFe concentrations decreased over time between sampling and filtering, the $\delta^{56}\text{Fe}$ value of dFe
484 decreased (*Fig. 4b*), consistent with oxidation of Fe(II) and precipitation of the Fe(III)-
485 (oxyhydr)oxides that form. It is important to note, however, that the oxidation half-life of Fe(II)
486 is significantly longer at E2 (1.45 to 5.63 h; *Lough et al., 2017*) than it is at Beebe (~ 0.28 h),
487 such that the number of oxidation half-lives between sampling and filtering of the sample from
488 the E2 plume was significantly lower (1-2 half-lives) than the number of oxidation half-lives
489 between sampling and filtering of the sample from the Beebe plume (> 10 half-lives). This
490 means that Fe(II) oxidation was continuing throughout the incubation at E2, but was essentially
491 complete by the time the first sub-sample was taken at Beebe.

492

493 5.6 Controls on the $\delta^{56}\text{Fe}$ signature of dissolved Fe in hydrothermal plumes

494 The key roles of iron sulfide and iron (oxyhydr)oxide formation on the evolution of the iron
495 isotopic composition of dFe as vent fluids mix with seawater on the Mid-Cayman ultra-slow
496 spreading ridge is consistent with observations made at other vent sites (e.g., *Bennett et al.*,
497 *2006*; *Rouxel et al.*, *2016*; *Fitzsimmons et al.*, *2017*; *Klar et al.*, *2017*; *Lough et al.*, *2017*;
498 *Nasemann et al.*, *2018*). **Fig. 5** compares the range of measured $\delta^{56}\text{Fe}$ values of dFe in
499 hydrothermal plumes published to date with the Fe/H₂S ratio of the end-member vent fluids
500 and the Fe(II) oxidation rate in overlying seawater. If the sample from Pele's Pit that represents
501 mixing between seawater and a low temperature fluid with high Mg is excluded, then there is
502 a general trend towards lower $\delta^{56}\text{Fe}$ values for dFe in the hydrothermal plume at vent sites that
503 have higher vent fluid Fe/H₂S (not significant at $P < 0.1$) and bottom waters that promote faster
504 Fe(II) oxidation rates (i.e. bottom waters with relatively high dissolved oxygen and high pH;
505 *Field and Sherrell*, *2000*) (significant at $P < 0.1$). The very low $\delta^{56}\text{Fe}$ values of dFe at Beebe
506 (as low as -4.08‰) reflect (i) the relatively high Fe/H₂S ratio (~ 1.2 - 1.7) of the vent fluids that
507 means that a greater proportion of vent fluid Fe escapes precipitation as Fe sulfide as the vent
508 fluids are expelled at the seabed and (ii) rapid conversion of Fe(II) to Fe(III) and precipitation
509 of Fe-(oxyhydr)oxides in the buoyant plume. While our new data suggest that spreading rate
510 therefore plays no obvious control on the Fe isotopic signature of dFe delivered to the neutrally
511 buoyant plume, and potentially into the ocean interior, the effects of Fe-binding organic ligands
512 on $\delta^{56}\text{Fe}$ as the plume evolves remain uncertain (*Toner et al.*, *2009*; *Fitzsimmons et al.*, *2017*).
513 There is a clear need for additional studies that quantify the iron isotopic signatures of the truly
514 dissolved (soluble) and colloidal iron fractions as well as longer term incubation experiments
515 that also measure the strength and concentration of iron-binding ligands.

516

517 **6 Conclusions**

518 This study investigated the chemical processes that regulate the evolution of the iron isotopic
519 signature of hydrothermal Fe during mixing between high-temperature vent fluids and seawater
520 at the Beebe and the Von Damm vent fields on the Mid-Cayman ultraslow-spreading ridge.
521 Hydrothermal vent fluids from Beebe had $\delta^{56}\text{Fe} = -0.28\text{‰}$, similar to other vent sites, whereas
522 vent fluids from Von Damm had slightly higher $\delta^{56}\text{Fe}$ (+0.08‰), likely due to precipitation of
523 Fe-sulfides that preferentially incorporate lighter Fe isotopes prior to venting at the seafloor.
524 At Beebe, around 50% of hydrothermal Fe precipitates as Fe-sulfides as soon as the vent fluids
525 are expelled at the seabed. Isotope data from incubation experiments on a Beebe buoyant plume
526 sample indicate that nanoparticulate Fe-sulfides can be carried upwards into the Beebe buoyant
527 plume, eventually coagulating and settling out over time.

528 At both sites, the $\delta^{56}\text{Fe}$ value of dFe in the early stages of buoyant plume formation was
529 significantly lower than the $\delta^{56}\text{Fe}$ value of the vent fluids (or background seawater), reaching
530 values of as low as -4.08‰ at Beebe and -2.49‰ at Von Damm. We show that this can be
531 principally attributed to oxidation of Fe(II) and precipitation of the Fe-(oxyhydr)oxides that
532 form. This is supported by analyses of the iron isotopic composition of TDFe; labile particulate
533 Fe is isotopically heavy ($\delta^{56}\text{Fe} = -0.13$ to $+0.71\text{‰}$) compared to the dFe, suggesting that labile
534 particulate Fe principally consists of Fe-(oxyhydr)oxides.

535

536 **Acknowledgements**

537 We thank the Master and crew of RRS *James Cook* cruise JC82 and the pilots and technical
538 team of the ROV *ISIS*. We also thank the editor and two anonymous reviewers for their
539 constructive comments that have improved the quality of this manuscript. This cruise was part
540 of the NERC-funded CayMin project (grant # NE/F01775811). WW's PhD studentship was

541 funded by the Chinese Scholarship Council and the University of Southampton. VC and AC
542 received support from CNRS-INSU grant *Post-Campagne: JC82 Cayman Ridge* and AL was
543 partly supported by NERC grant # NE/N010396/1.

544

545 **References**

- 546 Albarède, F., Beard, B., 2004. Analytical methods for non-traditional isotopes. *Reviews in*
547 *Mineralogy and Geochemistry*, 55(1), 113-152.
- 548 Anbar, A.D., Jarzecki, A.A. and Spiro, T.G., 2005. Theoretical investigation of iron isotope
549 fractionation between $\text{Fe}(\text{H}_2\text{O})_6^{3+}$ and $\text{Fe}(\text{H}_2\text{O})_6^{2+}$: Implications for iron stable isotope
550 geochemistry. *Geochimica et Cosmochimica Acta*, 69(4), 825-837.
- 551 Beard, B.L., Johnson, C.M., Von Damm, K.L., Poulson, R.L., 2003. Iron isotope constraints
552 on Fe cycling and mass balance in oxygenated Earth oceans. *Geology*, 31(7), 629-632.
- 553 Bennett, S.A., Rouxel, O., Schmidt, K., Garbe-Schönberg, D., Statham, P.J., German, C.R.,
554 2009. Iron isotope fractionation in a buoyant hydrothermal plume, 5°S Mid-Atlantic Ridge.
555 *Geochimica et Cosmochimica Acta*, 73(19), 5619-5634.
- 556 Bischoff, J.L., Dickson, F.W., 1975. Seawater-basalt interaction at 200°C and 500 bars:
557 implications for origin of sea-floor heavy-metal deposits and regulation of seawater chemistry.
558 *Earth and Planetary Science Letters*, 25(3), 385-397.
- 559 Boyd, P.W., Jickells, T., Law, C., Blain, S., Boyle, E., Buesseler, K., Coale, K., Cullen, J., De
560 Baar, H., Follows, M., 2007. Mesoscale iron enrichment experiments 1993-2005: Synthesis
561 and future directions. *Science*, 315(5812), 612-617.
- 562 Butler, I.B., Archer, C., Vance, D., Oldroyd, A., Rickard, D., 2005. Fe isotope fractionation on
563 FeS formation in ambient aqueous solution. *Earth and Planetary Science Letters*, 236(1), 430-
564 442.
- 565 Conway, T.M., John, S.G., 2014. Quantification of dissolved iron sources to the North Atlantic
566 Ocean. *Nature*, 511(7508), 212-215.
- 567 Connelly, D.P., Copley, J.T., Murton, B.J., Stansfield, K., Tyler, P.A., German, C.R., Van
568 Dover, C.L., Amon, D., Furlong, M., Grindlay, N., Hayman, N., 2012. Hydrothermal vent
569 fields and chemosynthetic biota on the world's deepest seafloor spreading centre. *Nature*
570 *Communications*, 3, 620. DOI: 10.1038/ncomms1636
- 571 Dideriksen, K., Baker, J. A., Stipp, S. L. S, 2008. Equilibrium Fe isotope fractionation between
572 inorganic aqueous Fe(III) and the siderophore complex, Fe(III)-desferrioxamine B. *Earth and*
573 *Planetary Science Letters*, 269, 280-290.

574 Dunlea A.G., Tegler L.A., Peucker-Ehrenbrink B., Anbar A.D., Romaniello S.J., Horner T.J.,
575 2021. Pelagic clays as archives of marine iron isotope chemistry. *Chemical Geology*, 575,
576 120201.

577 Field, M.P., Sherrell, R.M., 2000. Dissolved and particulate Fe in a hydrothermal plume at
578 9°45'N, East Pacific Rise: Slow Fe (II) oxidation kinetics in Pacific plumes. *Geochimica et*
579 *Cosmochimica Acta*, 64(4), 619-628.

580 Findlay, A.J., Estes, E.R., Gartman, A., Yücel, M., Kamyshny, A., Luther, G.W., 2019. Iron
581 and sulfide nanoparticle formation and transport in nascent hydrothermal vent plumes. *Nature*
582 *Communications*, 10(1), 1-7.

583 Fitzsimmons, J.N., Boyle, E.A., Jenkins, W.J., 2014. Distal transport of dissolved hydrothermal
584 iron in the deep South Pacific Ocean. *Proceedings of the National Academy of*
585 *Sciences*, 111(47), 16654-16661.

586 Fitzsimmons, J.N., John, S.G., Marsay, C.M., Hoffman, C.L., Nicholas, S.L., Toner, B.M.,
587 German, C.R., Sherrell, R.M., 2017. Iron persistence in a distal hydrothermal plume supported
588 by dissolved-particulate exchange. *Nature Geoscience*, 10(3), 195-201.

589 German, C.R., Campbell, A.C., Edmond, J.M., 1991. Hydrothermal scavenging at the Mid-
590 Atlantic Ridge: modification of trace element dissolved fluxes. *Earth and Planetary Science*
591 *Letters*, 107(1), 101-114.

592 Hodgkinson, M.R., Webber, A.P., Roberts, S., Mills, R.A., Connelly, D.P., Murton, B.J., 2015.
593 Talc-dominated seafloor deposits reveal a new class of hydrothermal system. *Nature*
594 *Communications*, 6. DOI: 10.1038/ncomms10150

595 Homoky, W.B., Severmann, S., Mills, R.A., Statham, P.J., Fones, G.R., 2009. Pore-fluid Fe
596 isotopes reflect the extent of benthic Fe redox recycling: evidence from continental shelf and
597 deep-sea sediments. *Geology*, 37(8), 751-754.

598 John, S.G., Adkins, J., 2012. The vertical distribution of iron stable isotopes in the North
599 Atlantic near Bermuda. *Global Biogeochemical Cycles*, 26(2). DOI: 10.1029/2011GB004043

600 Klar, J.K., James, R.H., Gibbs, D., Lough, A., Parkinson, I., Milton, J.A., Hawkes, J.A.,
601 Connelly, D.P., 2017. Isotopic signature of dissolved iron delivered to the Southern Ocean
602 from hydrothermal vents in the East Scotia Sea. *Geology*, 45(4), 351-354.

603 Kleint, C., Hawkes, J.A., Sander, S.G., Koschinsky, A., 2016. Voltammetric investigation of
604 hydrothermal iron speciation. *Frontiers in Marine Science*, 3, 75.

605 Lacan, F., Radic, A., Labatut, M., Jeandel, C., Poitrasson, F., Sarthou, G., Pradoux, C.,
606 Chemleff, J., Freydier, R., 2010. High-precision determination of the isotopic composition of
607 dissolved iron in iron depleted seawater by double spike multicollector-ICPMS. *Analytical*
608 *Chemistry*, 82(17), 7103-7111.

609 Lough, A., 2016. Trace metal chemistry of hydrothermal plumes. Doctoral dissertation,
610 University of Southampton.

611 Lough, A., Klar, J., Homoky, W., Comer-Warner, S., Milton, J., Connelly, D., James, R., Mills,
612 R., 2017. Opposing authigenic controls on the isotopic signature of dissolved iron in
613 hydrothermal plumes. *Geochimica et Cosmochimica Acta*, 202, 1-20.

614 Lough, A.J.M., Homoky, W.B., Connelly, D.P., Comer-Warner, S.A., Nakamura, K., Abyaneh,
615 M.K., Kaulich, B. and Mills, R.A., 2019a. Soluble iron conservation and colloidal iron
616 dynamics in a hydrothermal plume. *Chemical Geology*, 511 (225-237).

617 Lough, A.J.M., Connelly, D.P., Homoky, W.B., Hawkes, J.A., Chavagnac, V., Castillo, A.,
618 Kazemian, M., Nakamura, K.I., Araki, T., Kaulich, B., Mills, R.A., 2019b. Diffuse
619 hydrothermal venting: A hidden source of iron to the oceans. *Frontiers in Marine Science*, 6.
620 DOI: 10.3389/fmars.2019.00329

621 McDermott, J.M., 2015. Geochemistry of deep-sea hydrothermal vent fluids from the Mid-
622 Cayman Rise, Caribbean Sea. Doctoral dissertation, Massachusetts Institute of Technology.

623 McDermott, J.M., Sylva, S.P., Ono, S., German, C.R., Seewald, J.S., 2018. Geochemistry of
624 fluids from Earth's deepest ridge-crest hot-springs: Piccard hydrothermal field, Mid-Cayman
625 Rise. *Geochimica et Cosmochimica Acta*, 228, 95-118.

626 Morgan, J. L. L., Wasylenki, L. E., Nuester, J., Anbar, A. D. Fe isotope fractionation during
627 equilibration of Fe-organic complexes, 2010. *Environmental Science & Technology*, 44, 6095-
628 6101.

629 Nasemann, P., Gault-Ringold, M., Stirling, C.H., Koschinsky, A., Sander, S.G., 2018.
630 Processes affecting the isotopic composition of dissolved iron in hydrothermal plumes: A case
631 study from the Vanuatu back-arc. *Chemical Geology*, 476, 70-84.

632 Resing, J.A., Sedwick, P.N., German, C.R., Jenkins, W.J., Moffett, J.W., Sohst, B.M.,
633 Tagliabue, A., 2015. Basin-scale transport of hydrothermal dissolved metals across the South
634 Pacific Ocean. *Nature*, 523(7559), 200-203.

635 Rouxel, O., Dobbek, N., Ludden, J., Fouquet, Y., 2003. Iron isotope fractionation during
636 oceanic crust alteration. *Chemical Geology*, 202(1-2), 155-182.

637 Rouxel, O., Fouquet, Y., Ludden, J.N., 2004. Subsurface processes at the Lucky Strike
638 hydrothermal field, Mid-Atlantic Ridge: evidence from sulfur, selenium, and iron
639 isotopes. *Geochimica et Cosmochimica Acta*, 68(10), 2295-2311.

640 Rouxel, O., Shanks, W.C., Bach, W., Edwards, K.J., 2008. Integrated Fe- and S-isotope study
641 of seafloor hydrothermal vents at East Pacific Rise 9-10°N. *Chemical Geology*, 252(3), 214-
642 227.

643 Rouxel, O., Toner, B., Germain, Y., Glazer, B., 2018. Geochemical and iron isotopic insights
644 into hydrothermal iron oxyhydroxide deposit formation at Loihi Seamount. *Geochimica et*
645 *Cosmochimica Acta*, 220, 449-482.

646 Rouxel, O., Toner, B.M., Manganini, S.J., German, C.R., 2016. Geochemistry and iron isotope
647 systematics of hydrothermal plume fall-out at East Pacific Rise 9°50' N. *Chemical*
648 *Geology*, 441, 212-234.

649 Rudnicki, M.D., Elderfield, H., 1993. A chemical model of the buoyant and neutrally buoyant
650 plume above the TAG vent field, 26 degrees N, Mid-Atlantic Ridge. *Geochimica et*
651 *Cosmochimica Acta*, 57(13), 2939-2957.

652 Saito, M.A., Noble, A.E., Tagliabue, A., Goepfert, T.J., Lamborg, C.H., Jenkins, W.J., 2013.
653 Slow-spreading submarine ridges in the South Atlantic as a significant oceanic iron source.
654 *Nature Geoscience*, 6(9), 775-779.

655 Severmann, S., Johnson, C., Beard, B., German, C., Edmonds, H., Chiba, H., Green, D., 2004.
656 The effect of plume processes on the Fe isotope composition of hydrothermally derived Fe in
657 the deep ocean as inferred from the Rainbow vent site, Mid-Atlantic Ridge, 36°14' N. *Earth*
658 *and Planetary Science Letters*, 225(1), 63-76.

659 Severmann, S., Johnson, C.M., Beard, B.L., McManus, J., 2006. The effect of early diagenesis
660 on the Fe isotope compositions of porewaters and authigenic minerals in continental margin
661 sediments. *Geochimica et Cosmochimica Acta*, 70(8), 2006-2022.

662 Sharma, M., Polizzotto, M., Anbar, A., 2001. Iron isotopes in hot springs along the Juan de
663 Fuca Ridge. *Earth and Planetary Science Letters*, 194(1), 39-51.

664 Syverson, D.D., Borrok, D.M., Seyfried Jr, W.E., 2013. Experimental determination of
665 equilibrium Fe isotopic fractionation between pyrite and dissolved Fe under hydrothermal
666 conditions. *Geochimica et Cosmochimica Acta*, 122, 170-183.

667 Syverson, D.D., Luhmann, A.J., Tan, C., Borrok, D.M., Ding, K., Seyfried Jr, W.E., 2017. Fe
668 isotope fractionation between chalcopyrite and dissolved Fe during hydrothermal
669 recrystallization: an experimental study at 350° C and 500 bars. *Geochimica et Cosmochimica*
670 *Acta*, 200, 87-109.

671 Syverson, D.D., Pester, N.J., Craddock, P.R., Seyfried Jr, W.E., 2014. Fe isotope fractionation
672 during phase separation in the NaCl–H₂O system: An experimental study with implications for
673 seafloor hydrothermal vents. *Earth and Planetary Science Letters*, 406, 223-232.

674 Tagliabue, A., Bopp, L., Dutay, J.-C., Bowie, A.R., Chever, F., Jean-Baptiste, P., Bucciarelli,
675 E., Lannuzel, D., Remenyi, T., Sarthou, G., 2010. Hydrothermal contribution to the oceanic
676 dissolved iron inventory. *Nature Geoscience*, 3(4), 252-256.

677 Teng, F.Z., Dauphas, N., Huang, S., Marty, B., 2013. Iron isotopic systematics of oceanic
678 basalts. *Geochimica et Cosmochimica Acta*, 107, 12-26.

679 Toner, B.M., Fakra, S.C., Manganini, S.J., Santelli, C.M., Marcus, M.A., Moffett, J.W., Rouxel,
680 O., German, C.R., Edwards, K.J., 2009. Preservation of iron (II) by carbon-rich matrices in a
681 hydrothermal plume. *Nature Geoscience*, 2(3), 197-201.

682 Watson, A., Bakker, D., Ridgwell, A., Boyd, P., Law, C., 2000. Effect of iron supply on
683 Southern Ocean CO₂ uptake and implications for glacial atmospheric CO₂. *Nature*, 407(6805),
684 730-733.

685 Welch, S., Beard, B., Johnson, C., Braterman, P., 2003. Kinetic and equilibrium Fe isotope
686 fractionation between aqueous Fe (II) and Fe (III). *Geochimica et Cosmochimica Acta*, 67(22),
687 4231-4250.

688 Wu, L., Beard, B.L., Roden, E.E., Johnson, C.M., 2011. Stable iron isotope fractionation
689 between aqueous Fe (II) and hydrous ferric oxide. *Environmental Science & Technology*, 45(5),
690 1847-1852.

691 Yücel, M., Gartman, A., Chan, C.S., Luther III, G.W., 2011. Hydrothermal vents as a
692 kinetically stable source of iron-sulphide-bearing nanoparticles to the ocean. *Nature*
693 *Geoscience*, 4(6), 367-371.

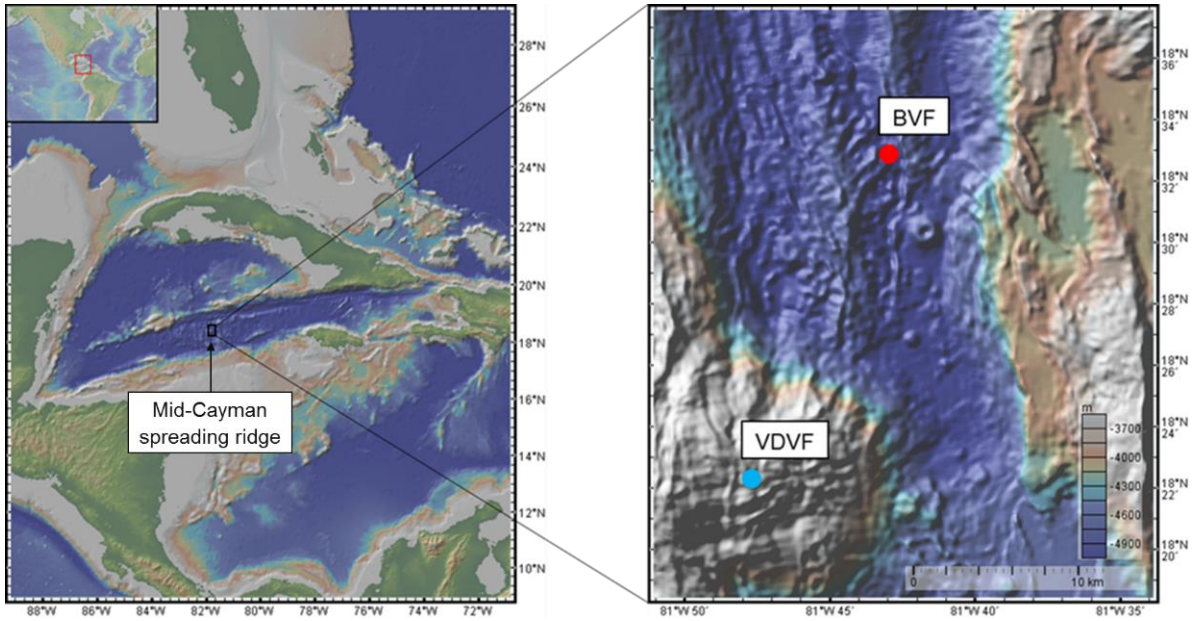
694

695 **Table 1** Composition of hydrothermal vent fluids from Beebe and Von Damm. NA = not
696 available; * calculated from all available data, which are given in the SI, except $\delta^{56}\text{Fe}$ which is
697 given as the value measured in the sample with lowest Mg. End-member uncertainty is the
698 computed standard error (1σ) on the Mg = 0 mM intercept (see text for details).

Sample	Vent site	Temp °C	pH	Mg mM	Cl mM	H ₂ S mM	Mn μM	Fe μM	Fe/ H ₂ S	$\delta^{56}\text{Fe}$ ‰
<i>Beebe vent field</i>										
FLU13	Beebe 125	401	3.1	2.7	371	NA	584	6168	NA	-0.28
FLU25	Beebe 125	401	3.1	5.7	388	3.2	527	NA	1.0	-0.06
FLU26	Beebe 125	401	3.0	3.1	378	3.2	537	5466	1.7	-0.08
<i>Beebe 125 end-member*</i>			2.8±1.1	0	366±5.8	3.8±0.3	597±10	6320±209	1.7	-0.28
FLU16	Deepest Vents	393	2.9	5.5	382	5.1	553	5744	1.1	-0.10
<i>Deepest Vents end-member*</i>			2.4±1.1	0	364±2.6	6.8±1.0	618±6	8150±1990	1.2	-0.10
<i>Beebe end-member (McDermott et al. 2018)</i>				0	356	12	567-571	6660-12800	0.6-1.0	
<i>Von Damm vent field</i>										
FLU1	Main Spire	215	6.0	15.1	659	0.95	8	18	0.02	0.08
<i>Main Spire Endmember*</i>			5.0±1.1	0	686±26	~1.6±0.3	11.6±0.44	22.1±3.9	~0.01	~0.08
FLU7	Hotter than Hole	133	6.1	26.9	613	0.45	12	292	0.6	-0.80
FLU8	Hotter than Hole	133	6.2	30.3	618	0.99	15	334	0.3	-0.36
FLU12	Chimlet 2	107	7.0	41.6	587	NA	10	145	NA	-0.90
<i>Hotter than Hole/ Chimlet 2 Endmember</i>			4.7±1.0	0	681±12	~1.2±0.4	22.5±4.2	412±137	~0.35	NA
FLU10	X15 marker	111	6.4	28.8	486	0.80	12	750	0.9	-0.58
<i>East Summit end-member (McDermott 2015)</i>		226	5.6	0	662	3.2	10	21	0.01	

699

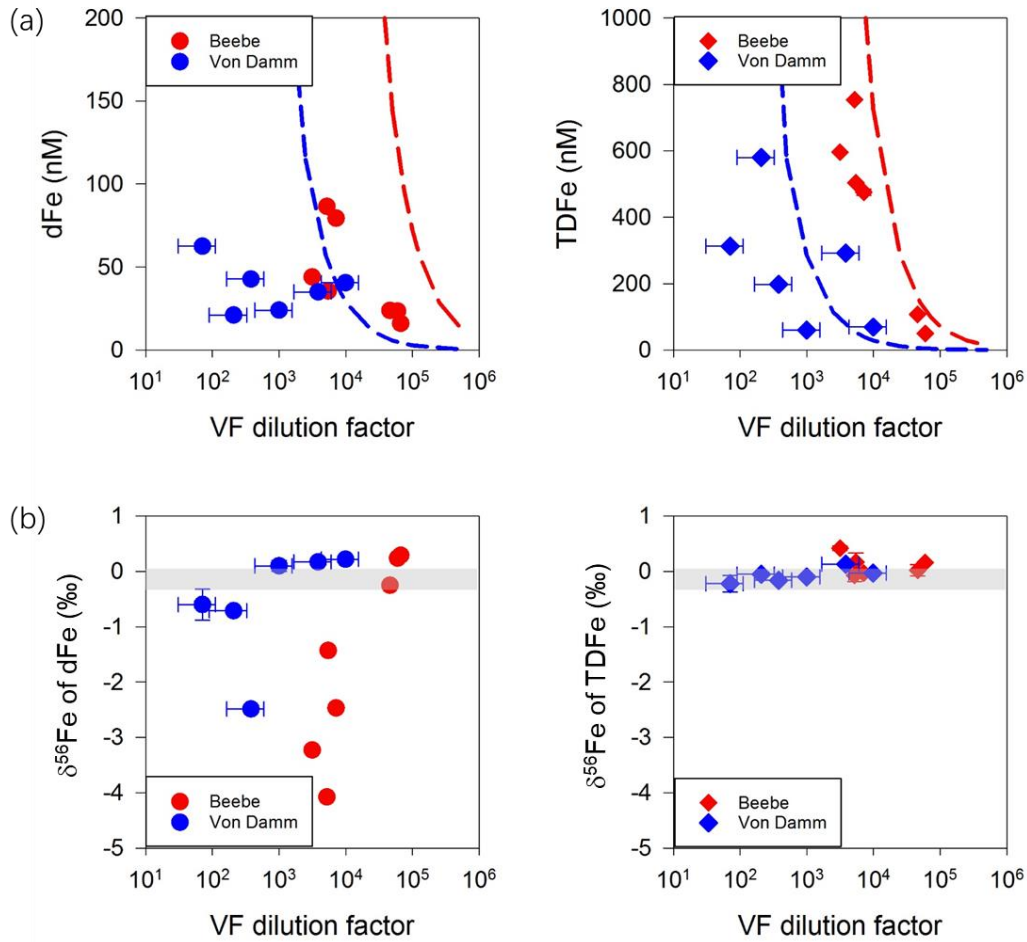
700



701

702 **Fig. 1** Location of the Beebe and Von Damm vent fields (respectively, BVF and VDVF) on the
 703 Mid-Cayman spreading ridge. Map courtesy of <http://www.geomapapp.org>

704



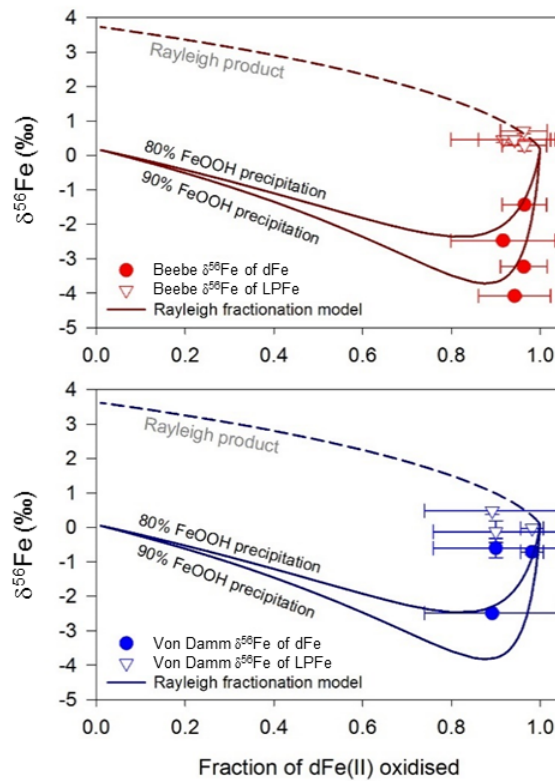
705

706 **Fig. 2 (a)** Concentrations of dissolved Fe (dFe) and total dissolvable Fe (TDFe), relative to
 707 vent fluid (VF) dilution factor at Beebe and Von Damm vent fields. The dashed lines show
 708 conservative mixing of the end-member fluid with background seawater, for Beebe (red) and
 709 Von Damm (blue). **(b)** Fe isotope compositions of dFe and TDFe (δ⁵⁶Fe of dFe and TDFe),
 710 relative to vent fluid dilution factor at Beebe and Von Damm. The grey band represents δ⁵⁶Fe
 711 of the lowest Mg vent fluids from both sites (see [Table 1](#)). Data are provided in the
 712 [Supplementary Information \(Table S2\)](#).

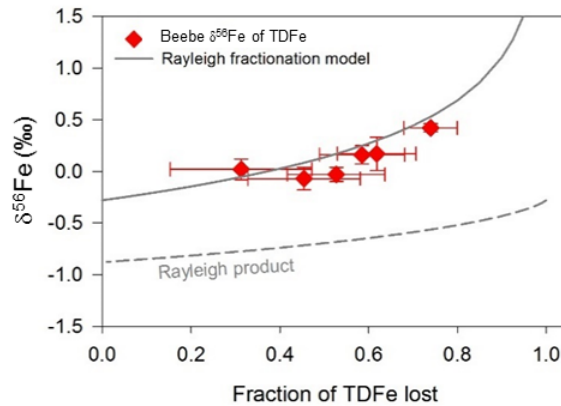
713

714

(a) Fe isotope fractionation during Fe(II)-Fe(III) oxidation



(b) Fe isotope fractionation during Fe-sulfide precipitation

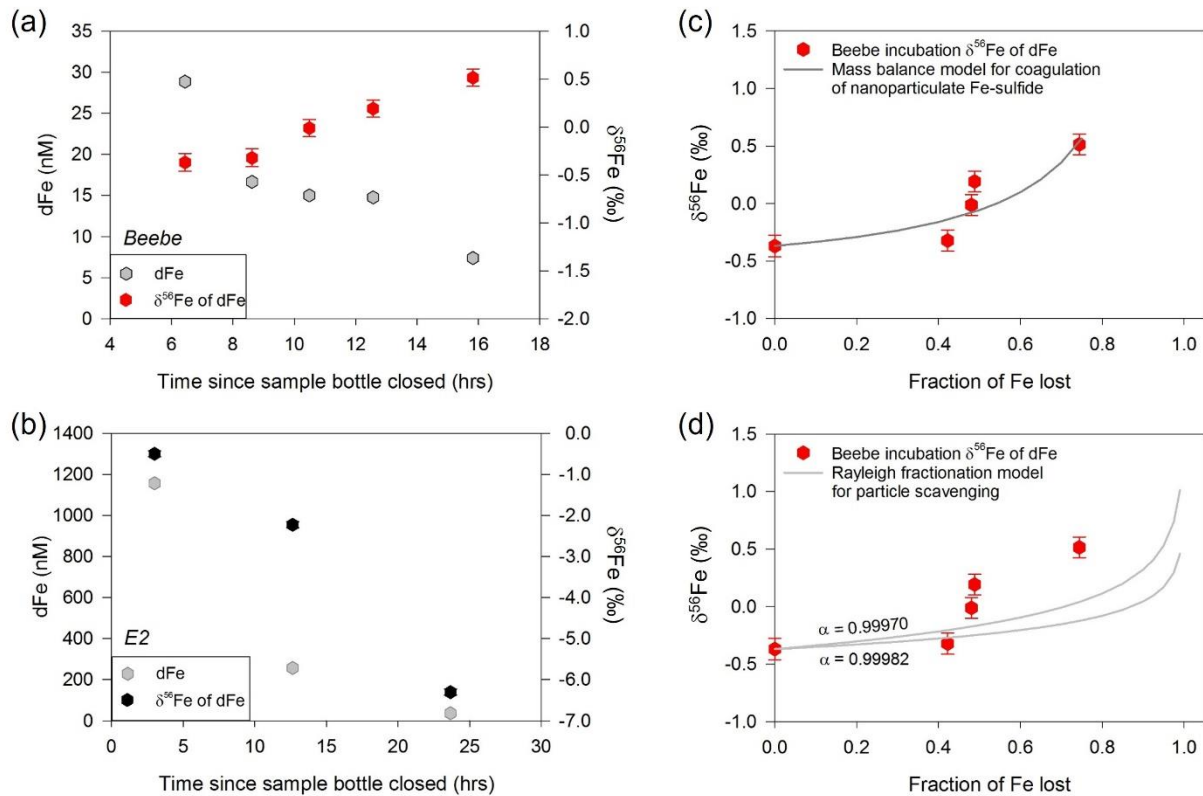


715

716 **Fig. 3 (a)** $\delta^{56}\text{Fe}$ relative to the fraction of dFe(II) oxidised to Fe(III). The observed $\delta^{56}\text{Fe}$ values
717 of dFe in the earliest stages of buoyant plume formation at Beebe and Von Damm are consistent
718 with a Rayleigh fractionation model with $\delta^{56}\text{Fe}(\text{III}) - \delta^{56}\text{Fe}(\text{II})_{\text{aq}} = 3.5\text{‰}$ (see text for details).
719 The calculated $\delta^{56}\text{Fe}$ values of labile particulate Fe are generally consistent or slightly lower
720 than predicted by the Rayleigh fractionation model. The horizontal error bars reflect the
721 uncertainty in the proportion of dFe(II) in the dFe pool (0 to 100%). **(b)** $\delta^{56}\text{Fe}$ relative to the
722 fraction of TDFe lost from the plume at Beebe. Solid line shows the evolution of $\delta^{56}\text{Fe}$ of TDFe
723 predicted by Rayleigh fractionation modelling of sulfide precipitation (see text for details). The

724 horizontal error bars reflect the uncertainty in the composition of the end-member fluid ([Table](#)
725 [S2](#)).

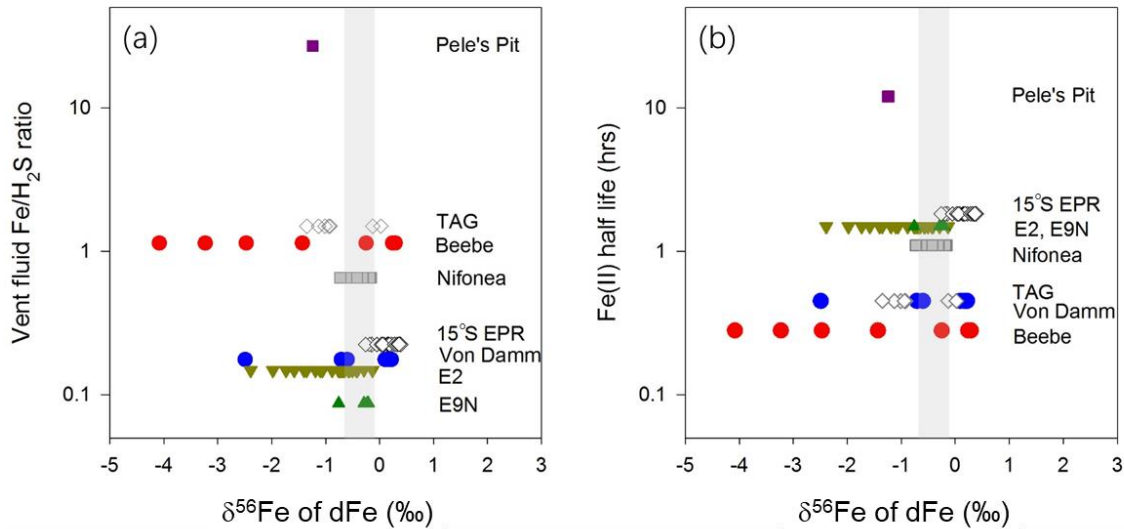
726



727

728 **Fig. 4 (a)** Change in dFe and $\delta^{56}\text{Fe}$ of dFe in the buoyant plume with time since the sample
 729 bottle was closed at Beebe, and **(b)** at E2 (*Lough et al., 2017*) for comparison. **(c and d)**
 730 Variation in $\delta^{56}\text{Fe}$ of dFe as a function of the proportion of dFe removed from solution over the
 731 course of the incubation experiment. Solid line in **(c)** shows results of a mass balance model
 732 for coagulation of Fe-sulfide nanoparticles that are assumed to constitute $\sim 75\%$ of the dFe
 733 fraction and have a distinct $\delta^{56}\text{Fe}$ of -0.68‰ (see text and [Table S3](#) for details). Solid line in
 734 **(d)** shows results of a Rayleigh fractionation model for particle scavenging, $\delta^{56}\text{Fe}_{\text{scavenged}} -$
 735 $\delta^{56}\text{Fe}_{\text{dFe}} = -0.18$ to -0.30‰ (see text for details).

736



737

738 **Fig. 5** Range of $\delta^{56}\text{Fe}$ values of dFe measured to date in hydrothermal plumes, compared to (a)
 739 vent fluid Fe/H₂S ratio and (b) Fe(II) half-life time. dFe isotope data are from: this study (Beebe
 740 and Von Damm); *Conway and John (2014)* (TAG on the Mid-Atlantic Ridge); *Lough et al.*
 741 *(2017)*, *Klar et al. (2017)* (E2 and E9N on the East Scotia Ridge); *Fitzsimmons et al. (2017)*
 742 *(15°S East Pacific Rise)*; *Nasemann et al. (2018)* (Nifonea at Vanuatu back-arc); *Rouxel et al.*
 743 *(2018)* (Pele's Pit at Loihi Seamount). Literature data, along with sources of vent fluid Fe/H₂S
 744 ratio and Fe(II) half-life, are given in the [Supplementary Information \(Table S5\)](#). Range in
 745 $\delta^{56}\text{Fe}$ of end-member hydrothermal fluids measured to date ([Table S4](#)) is shown by the vertical
 746 grey band.

747